

# Detection of a non-Gaussian Spot in WMAP

M. Cruz,<sup>1,2\*</sup> E. Martínez-González,<sup>1</sup> P. Vielva,<sup>3</sup> and L. Cayón<sup>4</sup>

<sup>1</sup>*IFCA, CSIC-Univ. de Cantabria, Avda. los Castros, s/n, 39005-Santander, Spain*

<sup>2</sup>*Dpto. de Física Moderna, Univ. de Cantabria, Avda. los Castros, s/n, 39005-Santander, Spain*

<sup>3</sup>*Physique Corpusculaire et Cosmologie, Collège de France, 11 pl. M. Berthelot, F-75231 Paris Cedex 5, France*

<sup>4</sup>*Department of Physics, Purdue University, 525 Northwestern Avenue, West Lafayette, IN 47907-2036, USA*

Accepted Received ; in original form

## ABSTRACT

An extremely cold and big spot in the WMAP 1-year data is analyzed. Our work is a continuation of a previous paper (Vielva et al. 2004) where non-Gaussianity was detected, with a method based on the Spherical Mexican Hat Wavelet (SMHW) technique. We study the spots at different thresholds on the SMHW coefficient maps, considering six estimators, namely number of maxima, number of minima, number of hot and cold spots, and number of pixels of the spots. At SMHW scales around  $4^\circ$  ( $10^\circ$  on the sky), the data deviate from Gaussianity. The analysis is performed on all sky, the northern and southern hemispheres, and on four regions covering all the sky. A cold spot at  $(b = -57^\circ, l = 209^\circ)$  is found to be the source of this non-Gaussian signature. We compare the spots of our data with 10000 Gaussian simulations, and conclude that only around 0.2% of them present such a cold spot. Excluding this spot, the remaining map is compatible with Gaussianity and even the excess of kurtosis in Vielva et al. 2004, is found to be due exclusively to this spot. Finally, we study whether the spot causing the observed deviation from Gaussianity could be generated by systematics or foregrounds. None of them seem to be responsible for the non-Gaussian detection.

**Key words:** methods: data analysis - cosmic microwave background

## 1 INTRODUCTION

The Cosmic Microwave Background (CMB) is the most ancient image of the universe. The measured temperature fluctuations reveal important characteristics of the primitive universe. Nowadays many models try to explain the primordial density fluctuations, and the key for deciding among them is the Gaussianity of the temperature fluctuations of the CMB. According to standard inflationary theories, these fluctuations are generated by a Gaussian, homogeneous and isotropic random field, whereas non-standard inflation (Linde & Mukhanov 1997, Peebles 1997, Bernardeau & Uzan 2002 and Acquaviva et al. 2003) and topological defect models (Turok & Spergel 1990 and Durrer 1999), predict non-Gaussian random fields.

Many difficulties have to be avoided in the Gaussianity analysis, since the temperature fluctuations may come from different sources, which should be identified. The primary fluctuations were originated on the last scattering surface (LSS), while secondary fluctuations were produced in the trip that CMB photons cover from the LSS to us. Some examples of the latter are the fluctuations caused by

the reionization of the universe (Ostriker & Vishniac 1986 and Aghanim et al. 1996), the Rees-Sciama effect (Rees & Sciama 1968 and Martínez-González & Sanz 1990), or gravitational lensing (Martínez-González et al. 1997, Hu 2000 and Goldberg & Spergel 1999). In addition we have systematic effects and contaminating foregrounds, like the Galactic emissions or extragalactic point sources, which have to be considered in the Gaussianity study.

In the last years, many groups have published analysis of Gaussianity. The Wilkinson Microwave Anisotropy Probe (WMAP) 1-year all-sky data (Bennett et al. 2003a), were found to be consistent with Gaussianity by the WMAP science team (Komatsu et al. 2003). A measure of the phase correlations of temperature fluctuations (taking several combinations of the bispectrum into account), and the Minkowski functionals, were used in the latter paper. Thereafter several other groups have found non-Gaussian signatures or asymmetries in the WMAP data (Park 2003, Eriksen et al. 2003, 2004a, Hansen et al. 2004a, b). Several methods were used including Minkowski functionals,  $N$ -point correlation functions, or local curvature methods. Also some other works such as Chiang et al. 2003 and Copi et al. 2003, detect deviations from Gaussianity, using the Internal Linear Combination (ILC) map (Bennett et al. 2003a) and other

\* e-mail: cruz@ifca.unican.es

maps, derived from the WMAP data. (However, the use of the ILC map is not recommended by the WMAP team, because of their complex noise and foreground properties).

Our basic reference is Vielva et al. 2004, where a non-Gaussian detection in the WMAP 1-year data was reported. Convoluting the data with the SMHW, an excess of kurtosis was found at scales around  $4^\circ$ , involving a size on the sky close to  $10^\circ$ . The deviation from Gaussianity presented an upper tail probability of 0.4%. This deviation was localized in the southern hemisphere and an extremely cold spot at  $b = -57^\circ$ ,  $l = 209^\circ$ , was regarded as a possible source of the non-Gaussianity (we call it *The Spot*).

Mukherjee & Wang 2004 have carried out an extrema analysis using the SMHW, finding an excess of cold pixels in all the sky at the same scales as Vielva et al. 2004. In the present paper, our aim is to localize the non-Gaussianity, specifying whether The Spot alone is the origin of the detection, and to study all the spots of the data in order to quantify how atypical The Spot under a Gaussian model is.

Also recently, Larson & Wandelt 2004 have carried out an extrema analysis in real space, finding non-Gaussian evidences.

The present paper is organized as follows. In §2 we describe the data and simulations used to study the Gaussianity. The wavelet technique and the estimators are explained in §3. The results of our work are presented in §4. In §5 we discuss the possible sources of the non-Gaussian detection and in §6 we present the conclusions of our results.

## 2 DATA AND SIMULATIONS

We have followed a similar procedure as in Vielva et al. 2004. Hence our data are the 1-year WMAP data, available in the *Legacy Archive for Microwave Background Data Analysis* (LAMBDA) web page <sup>†</sup>, choosing for our analysis the combined Q-V-W map. The WMAP receivers, take their observations at 5 frequency bands, namely K-band (22.8 GHz, 1 receiver), Ka-Band (33.0 GHz, 1 receiver), Q-Band (40.7 GHz, 2 receivers), V-Band (60.8 GHz, 2 receivers) and W-Band (93.5 GHz, 4 receivers). The combined map is a linear combination of the receivers where CMB is the dominant signal, namely Q, V, W radiometers:

$$T(\mathbf{x}) = \sum_{j=3}^{10} T_j(\mathbf{x}) w_j(\mathbf{x}), \quad (1)$$

The Q-Band receivers are denoted with indices  $j = 3, 4$ , V-Band receivers with indices  $j = 5, 6$ , whereas indices  $j = 7, 8, 9, 10$  correspond to the four W-Band receivers. Noise weights  $w_j(\mathbf{x})$  are defined so that receivers with less noise have more weight:

$$w_j(\mathbf{x}) = \frac{\bar{w}_j(\mathbf{x})}{\sum_{j=3}^{10} \bar{w}_j(\mathbf{x})}, \quad \bar{w}_j(\mathbf{x}) = \frac{N_j(\mathbf{x})}{\sigma_{0j}^2} \quad (2)$$

where  $\sigma_{0j}$  is the noise dispersion per observation and  $N_j(\mathbf{x})$  is the number of observations performed by the receiver  $j$  at position  $\mathbf{x}$  (see Bennett et al. 2003a). Foregrounds are corrected for each receiver, using the foreground template

described in Bennett et al. 2003b. The combined map increases the signal to noise ratio.

The Hierarchical, Equal Area and iso-Latitude Pixelization (HEALPix, Górski et al. 1999) is used in all maps. The resolution parameter of the original map, is  $N_{side} = 512$  but we have degraded it to  $N_{side} = 256$ , since very small scales are dominated by noise. Afterwards the *Kp0* mask was applied in order to get rid of foreground or point source contaminated pixels. This mask removes 23.2% of the pixels, especially the strongly contaminated pixels around the Galactic plane. Finally, the residual monopole and dipole outside the mask are subtracted. The mask and the foreground cleaned frequency maps can be found in the LAMBDA site.

Following the same procedure as in Vielva et al. 2004, we have produced 10000 Gaussian simulations with the purpose of checking the Gaussianity of the data. Starting with the cosmological parameters estimated by the WMAP team (Table 1 of Spergel et al. 2003), we have calculated the  $C_\ell$  using CMBFAST (Seljak & Zaldarriaga 1996). We have generated random Gaussian  $a_{\ell m}$  of CMB realizations and convolved them with the adequate beam for each receiver. After transforming from harmonic to real space, uncorrelated Gaussian noise realizations have been added, taking into account the number of observations per pixel ( $N_j(\mathbf{x})$ ) and the noise dispersion per observation ( $\sigma_{0j}$ ). At this point the simulations were degraded to  $N_{side} = 256$  and the *Kp0* mask has been applied. At the end, monopole and dipole are subtracted outside the mask

In the present work we have studied the spots above or below a given threshold  $\nu$ , therefore we have normalized the data and the simulations, dividing each map by its dispersion, after subtracting the mean.

## 3 WAVELETS AND ESTIMATORS

Several works have been published in recent years concerning CMB studies based on wavelets. Wavelet transforms can be applied to separate the different components appearing in microwave observations (Tenorio et al. 1999, Cayón et al. 2000, Vielva et al. 2001a, Vielva et al. 2001b and Vielva et al. 2003a), in denoising techniques (Sanz et al. 1999a,b) and in Gaussianity studies (Pando et al. 1998, Hobson et al. 1999, Aghanim et al. 2003, Barreiro et al. 2000, Barreiro & Hobson 2001 and references listed below for the spherical symmetry). Wavelets increase the signal to noise ratio, allowing us to detect weak non-Gaussian signals. Furthermore they preserve the spatial location and the angular scale  $R$  of a hypothetical non-Gaussian feature. This is a very important advantage since our main goal in this paper is to study the hot and cold spots over several thresholds.

In our case, the ideal wavelet is the SMHW (Antoine J. P. & Vanderheynt P. 1998), which has been applied to non-Gaussian studies of the COBE-DMR data (Cayón et al. 2001, 2003), to *Planck* simulations (Martínez-González et al. 2002) and to the 1-year WMAP data in our basic reference (Vielva et al. 2004). The SMHW optimally enhances the non-Gaussian signatures on the sphere (Martínez-González et al. 2002). The expression of the SMHW is:

$$\Psi_S(y, R) = \frac{1}{\sqrt{2\pi N(R)}} \left[ 1 + \left( \frac{y}{2} \right)^2 \right]^2 \left[ 2 - \left( \frac{y}{R} \right)^2 \right] e^{-y^2/2R^2}, \quad (3)$$

<sup>†</sup> <http://www.cmbdata.gsfc.nasa.gov/>

where  $R$  is the scale and  $N(R)$  is a normalization constant:  $N(R) \equiv R\sqrt{1 + R^2/2 + R^4/4}$ . The distance  $y$  on the tangent plane is related to the polar angle ( $\theta$ ) as:  $y \equiv 2 \tan \theta/2$ . Data and simulations have been convolved with the SMHW at different scales, to obtain the SMHW coefficient maps analyzed in this work. The study has also been performed in the data and simulations previous to the convolution with the SMHW. These maps are referred to as maps in real space, at scale  $R_o$ .

We have considered the following six estimators: number of maxima, number of minima, number of hot spots, number of cold spots, number of hot pixels (hot area) and number of cold pixels (cold area). All of them are referred to a particular threshold; thus maxima, hot spots and hot pixels lie above a threshold  $\nu$ , whereas number of minima, cold spots and cold pixels lie below  $-\nu$ . The analysis has been done in seven regions: all sky, northern hemisphere, southern hemisphere, Northeast ( $b > 0, l < 180$ ), Northwest ( $b > 0, l > 180$ ), Southeast ( $b < 0, l < 180$ ) and Southwest ( $b < 0, l > 180$ ). Each region has its own dispersion and has to be normalized separately.

#### 4 THE ANALYSIS

The first step in our analysis is the convolution of data and simulations with the SMHW at 15 scales ( $R_1 = 13.7$ ,  $R_2 = 25$ ,  $R_3 = 50$ ,  $R_4 = 75$ ,  $R_5 = 100$ ,  $R_6 = 150$ ,  $R_7 = 200$ ,  $R_8 = 250$ ,  $R_9 = 300$ ,  $R_{10} = 400$ ,  $R_{11} = 500$ ,  $R_{12} = 600$ ,  $R_{13} = 750$ ,  $R_{14} = 900$  and  $R_{15} = 1050$  arcmin). Since the convolution mixes up pixels of the masked region with unmasked pixels, the resulting map has many corrupted SMHW coefficients. This effect involves a loss of efficiency, so we applied an additional mask as explained in Vielva et al. 2004, extending the  $Kp\theta$  mask to  $2.5 R$ . The results in Vielva et al. 2004 were shown to be quite independent of the definition of this extended mask. For each map we have calculated the estimators on the seven previously described regions. The chosen thresholds are  $\pm 2.0$ ,  $\pm 2.5$ ,  $\pm 3.0$ ,  $\pm 3.5$ ,  $\pm 4.0$  and  $\pm 4.5$ . In the figures we have represented only absolute values for the thresholds, recalling that for cold spots and minima, values lie below a negative threshold, whereas hot spots and maxima values lie above a positive threshold.

Once the estimators were calculated for data and simulations, we proceeded to establish acceptance intervals at significance levels  $\alpha$  (32%, 5% and 1%). Therefore we have sorted the 10000 values of each estimator into ascending numbers and excluded  $10000\alpha/2$  values from each tail of the distribution. The two limiting values, corresponding to simulations  $1 + 10000\alpha/2$  and  $10000(1 - \alpha/2)$  define the acceptance interval containing a probability of  $1 - \alpha$ . The remaining probability is  $\alpha/2$  above and below the interval. In all figures this acceptance intervals are plotted, the 32% interval corresponds to the inner band, the 5% interval to the middle band and the 1% significance level, to the outer one.

The results for the different regions are presented in the next three subsections.

##### 4.1 All sky, North and South

Deviations from Gaussianity have been detected at scales  $R_5$ ,  $R_8$  and  $R_9$ . For threshold 3.0, the results are repre-

sented in Figure 1. At scale  $R_5$  the hot area lies outside the 99% acceptance interval. However we have studied this case carefully, noting that this threshold is the only one where data lie outside the intervals, whereas the number of hot spots and number of maxima do not depart from Gaussianity, even at this scale. Dividing the sky into two hemispheres we checked that this was not a localized effect either. Even contiguous scales were compatible with Gaussianity, hence we concluded that this non-Gaussian feature was not significant.

On the contrary, in the case of cold areas, deviations are observed at scales  $R_8$  and  $R_9$  at several thresholds as can be seen in Figure 2. We represent in Figure 2 the number of cold spots, cold area and number of minima, for all considered thresholds at scales  $R_8$  and  $R_9$ , in order to observe what is happening there with more detail. The number of minima and cold spots was exactly one at thresholds 4.0 and 4.5, reaching the borderline of our 99% acceptance interval. For the number of cold spots, at threshold 4.0 for scale  $R_8$  and thresholds 3.5 and 4.0 for scale  $R_9$ , the 95% and 99% acceptance intervals coincide. This can happen when the number of spots is very low. Consider for example a binomial distribution where the number of spots can only take values 0 or 1. The way we define the acceptance intervals determines that for such cases some of these intervals must coincide. The most striking non-Gaussian signature was found for the cold area at scales  $R_8$  and  $R_9$  where the data exhibited an extremely high number of cold pixels at thresholds over 3. The cold area lies outside the 99% acceptance interval at thresholds above 3.0 in the two scales presented in Figure 2.

At thresholds 4.0 and 4.5 the mentioned observations reveal that the non-Gaussianity is only due to one particular spot, which reaches a minimum value of  $-4.7\sigma$  at ( $b = -57^\circ, l = 209^\circ$ ) and scale  $R_9$ . At lower thresholds several spots contribute to the observed deviation. A precise analysis of The Spot is presented in the following sections. The data suggest that we are dealing with a very cold and big spot. These results agree with the results reported in Vielva et al. 2004, since the non-Gaussianity has been detected at the same scales. The hot spots did not show any non-Gaussian evidence. Furthermore, subtracting the cold pixels from the hot pixels, a strong hot-cold asymmetry was revealed at scales  $R_8$ ,  $R_9$  and  $R_{10}$ , see Figure 3. The lower tail probabilities displayed in Table 1 show non-Gaussian values of up to 99.85%.

Our purpose was to locate the non-Gaussian sources. We studied the northern and southern hemispheres separately, expecting to find non-Gaussian results in the southern hemisphere because The Spot is located there. Results presented in Figure 4 show that the northern hemisphere is compatible with the Gaussian simulations whereas the southern hemisphere shows a clear deviation from the acceptance intervals. To show the North-South asymmetry, the number of hot and cold pixels in the South were subtracted from the Northern ones. Results are presented in Figure 5. Deviations from Gaussianity can be clearly observed in the number of cold pixels at thresholds 3.0 and above. Previous works such as Vielva et al. 2004, Eriksen et al. 2004a or Hansen 2004b have already reported North-South asymmetries, which are confirmed here.

The marked observed asymmetry, prompted us to di-

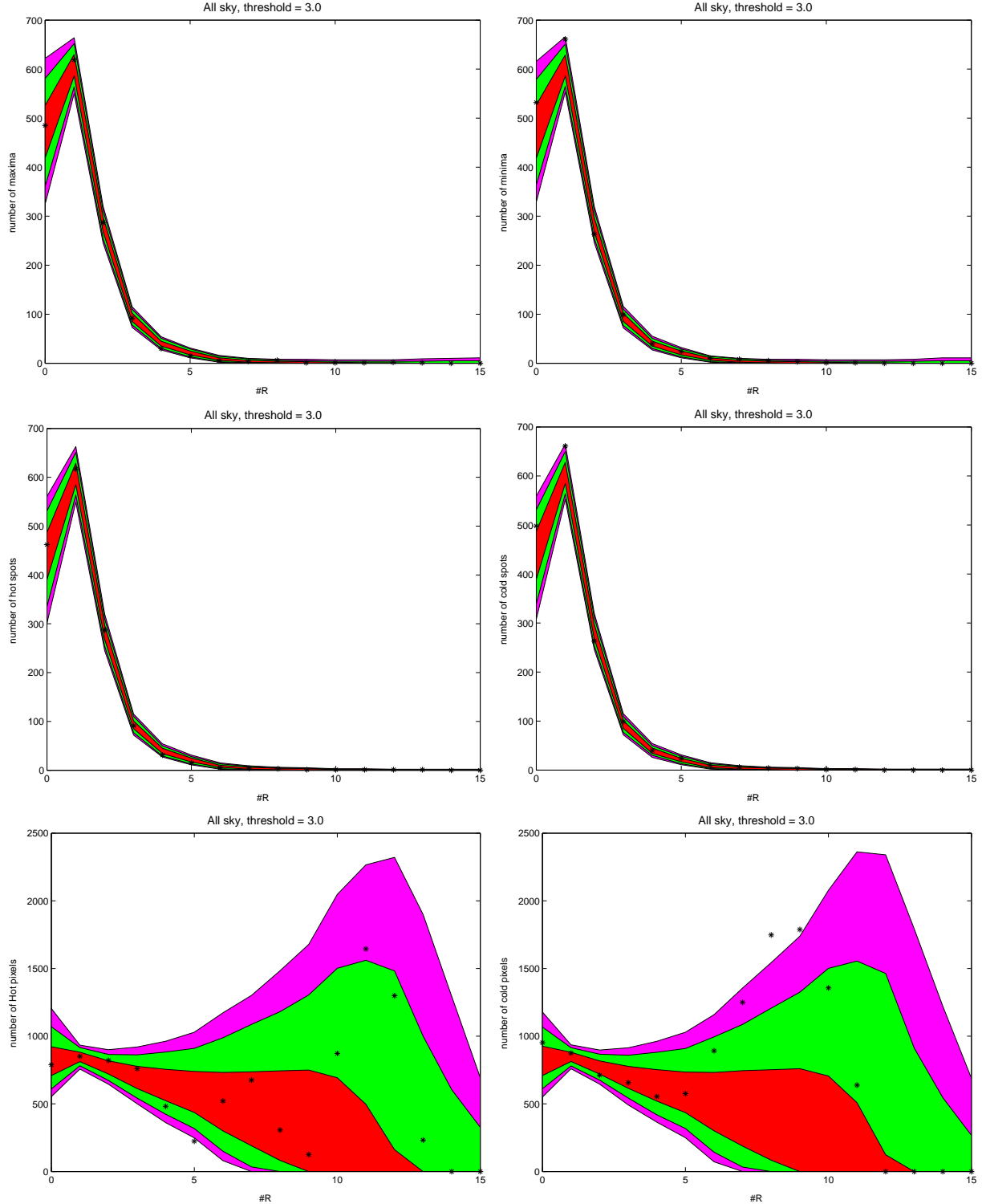


**Figure 1.** This figure shows from left to right and top to bottom, number of maxima, number of minima, number of hot spots, number of cold spots, hot and cold area for each of the considered scales at threshold 3.0. Scale  $R_0$  corresponds to real space. The combined map values are plotted as asterisks. The acceptance intervals for the 32% (inner), 5% (middle) and 1% (outer) significance levels, given by the 10000 simulations are also plotted. Non-Gaussianity is found at scales  $R_5$  in the hot area,  $R_8$  and  $R_9$  in the cold area. At other scales the data always lie at least within the 99% acceptance band. For scale  $R_5$  the deviation occurs only for this threshold and scale whereas scales  $R_8$  and  $R_9$  show a more significant detection.

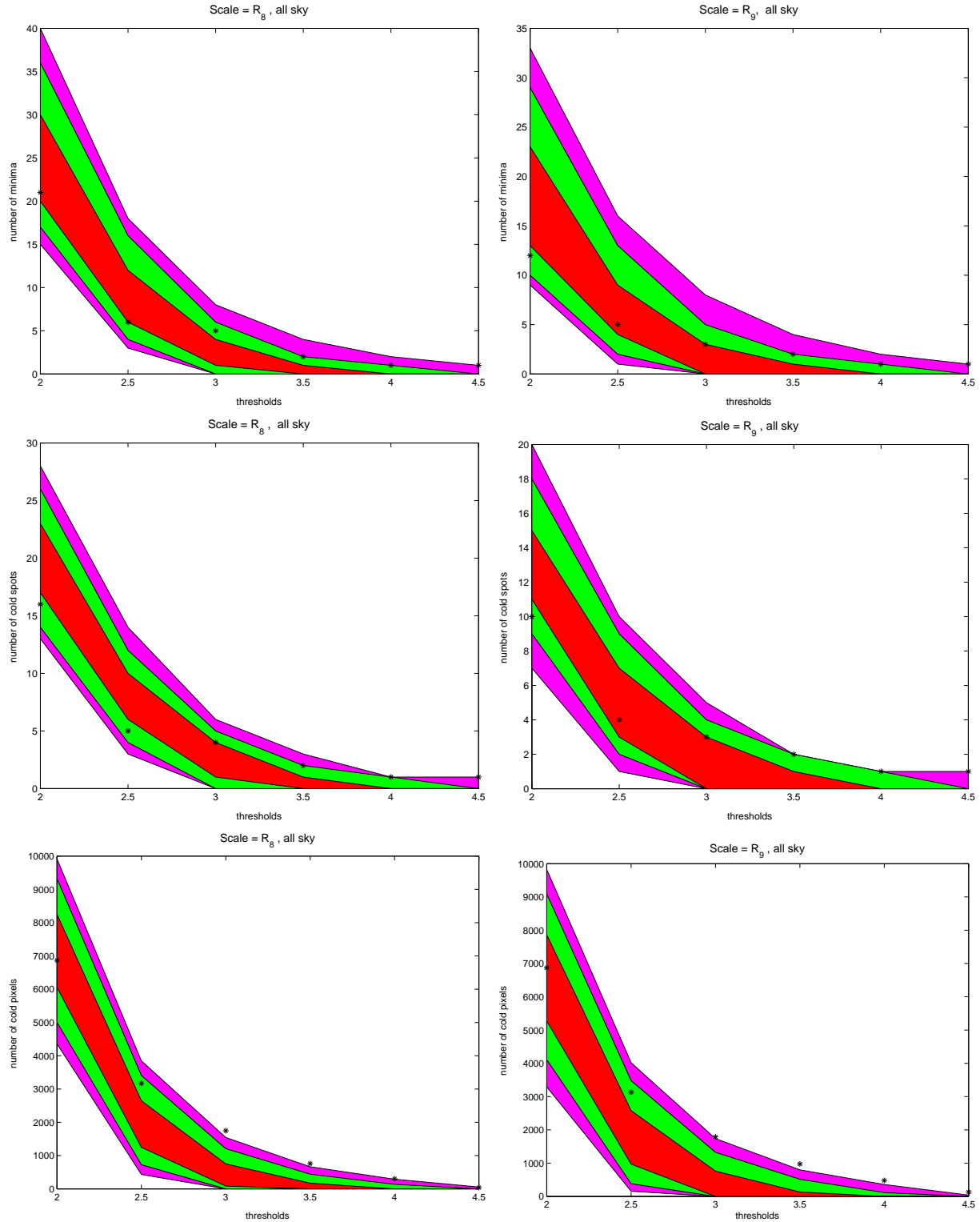


**Figure 2.** Number of minima, number of cold spots and cold area are shown for scale  $R_8$  at the left column and scale  $R_9$  at the right column. As in figure 1 the asterisks represent the combined WMAP data, and the acceptance intervals for the 32% (inner), 5% (middle) and 1% (outer) significance levels, given by the 10000 simulations are also shown. The data lie outside the acceptance intervals for the area, at thresholds over 3.0. The borderline of the 5% and 1% acceptance intervals coincide at some high thresholds for the number of spots, because at this scales the number of spots is very low.

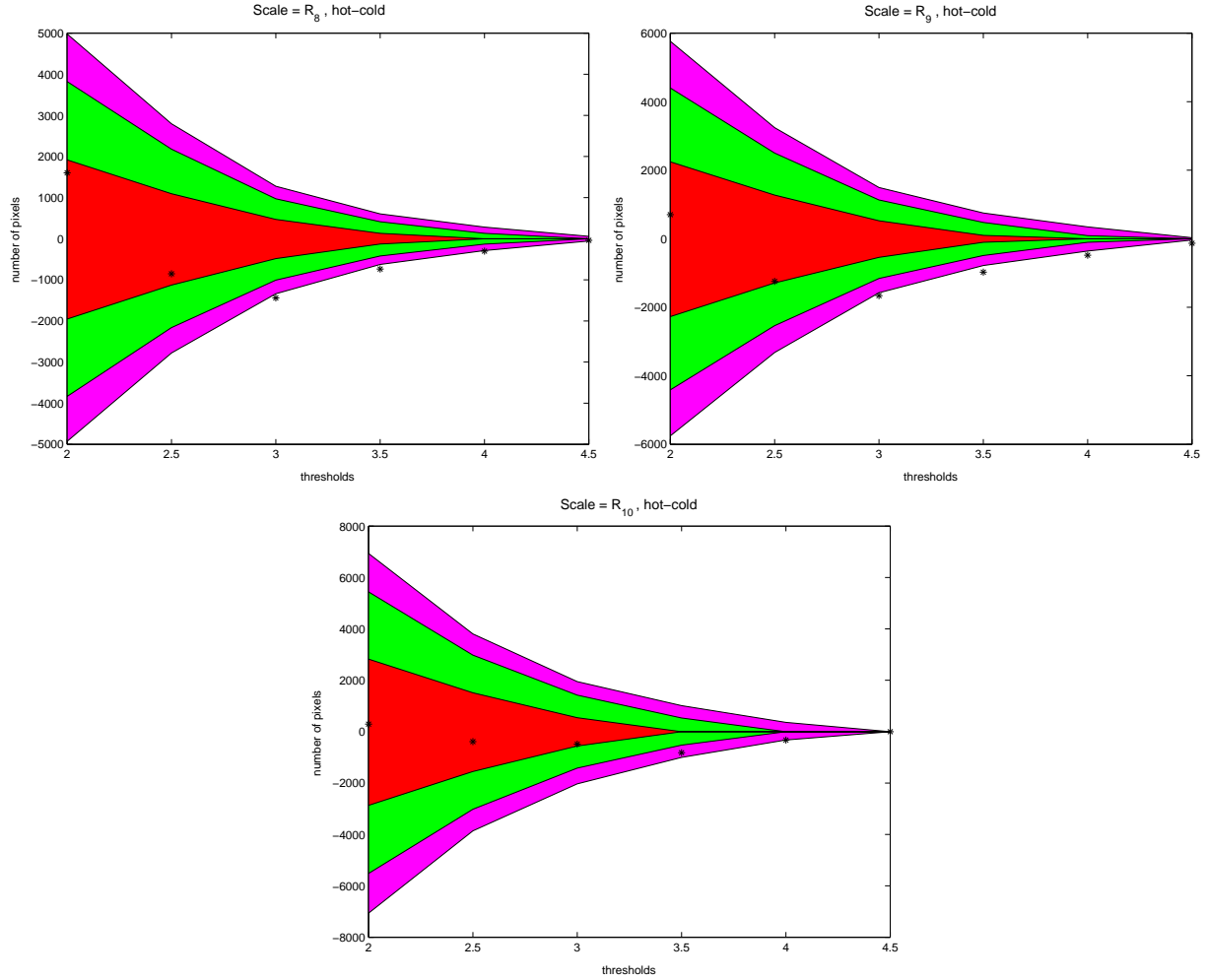


**Figure 3.** Hot-cold asymmetry, in the area. The excess of cold pixels at scales  $R_8$ ,  $R_9$  and  $R_{10}$  happens at high thresholds. Data and acceptance intervals are represented in the same manner as in previous figures.

Scale	threshold	probability
$R_8$	3.0	0.37%
	3.5	0.26%
	4.0	0.44%
	4.5	0.65%
$R_9$	3.0	0.39%
	3.5	0.15%
	4.0	0.19%
	4.5	0.22%
$R_{10}$	3.0	18.22%
	3.5	1.04%
	4.0	0.48%

**Table 1.** Lower tail probabilities of having the hot-cold asymmetry (in the number of pixels) of our data under a Gaussian model, at different scales and thresholds. Most of the values are below 1%. At scale  $R_{10}$  and threshold 4.5 the number of hot and cold pixels are both zero, because the threshold is too high and therefore we do not show this threshold for the mentioned scale.

vide the sky into four regions with the purpose of studying a Southeast-Southwest asymmetry.

## 4.2 Four regions

We analyzed four regions independently by splitting each hemisphere into two parts,  $l < 180$  (East) and  $l > 180$  (West). The results presented in Figure 6 clearly reveal the location of the non-Gaussian signatures. The Southwest is the only region where the data lie outside the acceptance intervals. As expected, the region containing The Spot is not compatible with Gaussianity, whereas the other three regions are compatible with a Gaussian behaviour. Note that although Eriksen et al. 2004b found the ILC weights to have particular values in this region, this does not affect our results since we use the combined, cleaned Q-V-W map.

In the next section we quantify the significance of The Spot.

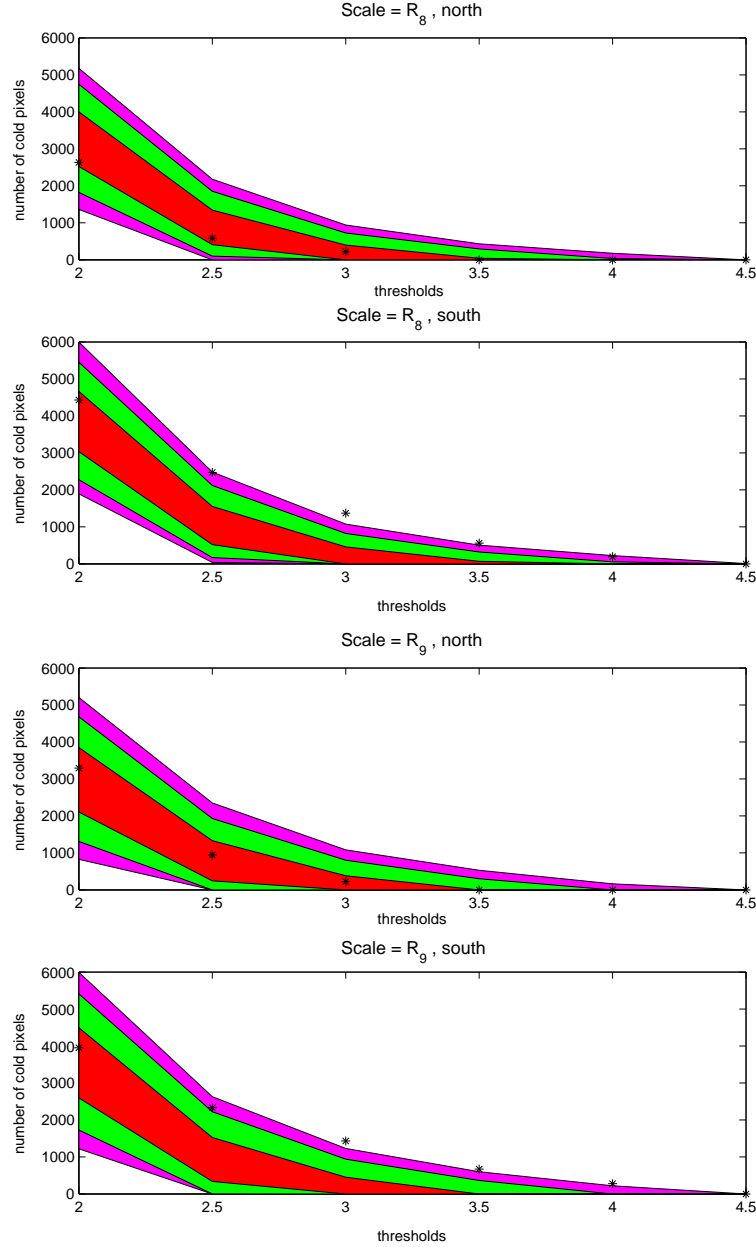


**Figure 4.** Cold area in the northern and southern hemispheres at scales  $R_8$  and  $R_9$ . The southern hemisphere shows a non-Gaussian behaviour. Again we represent data and acceptance intervals as in Figure 1.

### 4.3 The Spot

Our aim in this section is to quantify the probability of finding a spot like the one found at  $(b = -57^\circ, l = 209^\circ)$  in a Gaussian, homogeneous and isotropic random field, and to check whether the map without The Spot is compatible with Gaussianity or not. Comparing The Spot with the biggest cold spot of each simulation we can estimate the probability of observing such a spot for the Gaussian model. We show the histograms with the biggest cold spot of each simulation at threshold 3.0 and scales  $R_8$  and  $R_9$  in Figure 7. The results for all thresholds are summarized in Table 2. Note that some simulations do not have any spots at high thresholds and hence they do not appear in the histograms but

we take them into account to estimate the probabilities. All probabilities are below 0.7%. The lowest value is 0.18% and implies a non-Gaussian detection at the 99.82% level.

At this point we can make the hypothesis that the data could be explained as the sum of a Gaussian, homogeneous and isotropic random field, plus a non-Gaussian spot which is not generated by this field. With the purpose of checking our hypothesis, we have compared the cold area of data and simulations, at scales  $R_8$ ,  $R_9$  and thresholds 3.0, 3.5 where the data present more than one spot. First we have estimated the upper tail probabilities of finding the total cold area (including all cold spots), counting how many simulations present a greater or equal cold area, obtaining very

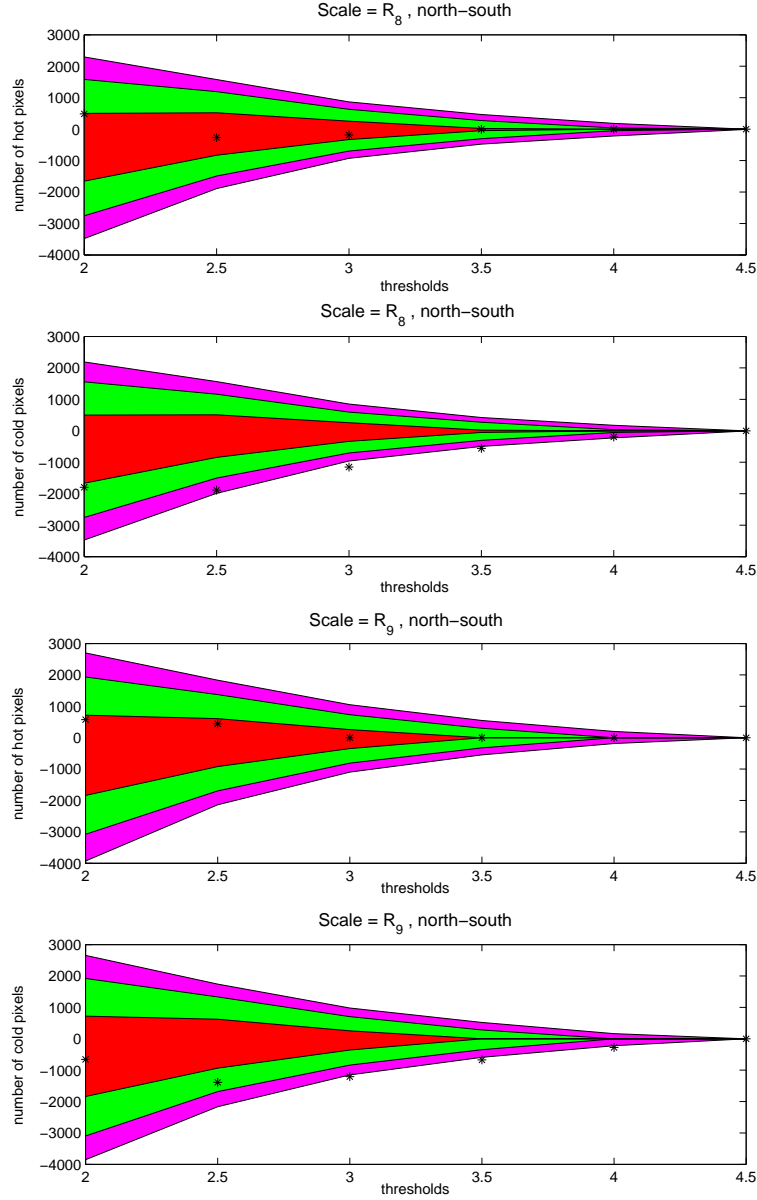


**Figure 5.** The two upper panels represent the North-South asymmetry for hot and cold area, at scale  $R_8$  and the two panels below, the mentioned asymmetries at scale  $R_9$ . The southern hemisphere shows an excess of cold pixels. Acceptance intervals and data are represented as in previous figures.

low values (see Table 3). If we subtract The Spot from the cold area in the data, and calculate again the probabilities, we appreciate how the remaining area is compatible with Gaussianity, since the upper tail probabilities grow in a factor of 100. This result is represented in Figure 8. The line on the right hand side is the total cold area of the data whereas the one on the left hand side is the area remaining after subtracting The Spot. The increase in probability can easily be appreciated. Here we should have considered that we were using fewer pixels in the data than in the simulations because The Spot has been subtracted only in the data. But since these pixels represent only about 0.5% of the total pixels at scales  $R_8$  and  $R_9$ , we can neglect them, without modifying substantially the results. Hence regard-

ing The Spot as a non-Gaussian outlier, the remaining data are compatible with Gaussianity.

To finish this section, we want to remark some characteristics of The Spot. Before convolving the combined map, The Spot appears as several smaller, resolved spots with a minimum temperature of  $-398\mu K$  at  $(b = -56^\circ, l = 210^\circ)$ . The average value of the four most prominent spots, listed in table 4 is  $-348\mu K$ . However, these four spots are not exclusively responsible for The Spot, since removing them, the mean value of the remaining pixels forming The Spot, is close to  $-1\sigma$ . We have filtered the combined map with a Gaussian of scale  $4^\circ$ , the characteristic scale given by the SMHW analysis. The Spot appears with an amplitude of  $-78\mu K$  at  $(b = -56^\circ, l = 210^\circ)$  as summarized in Table 4.

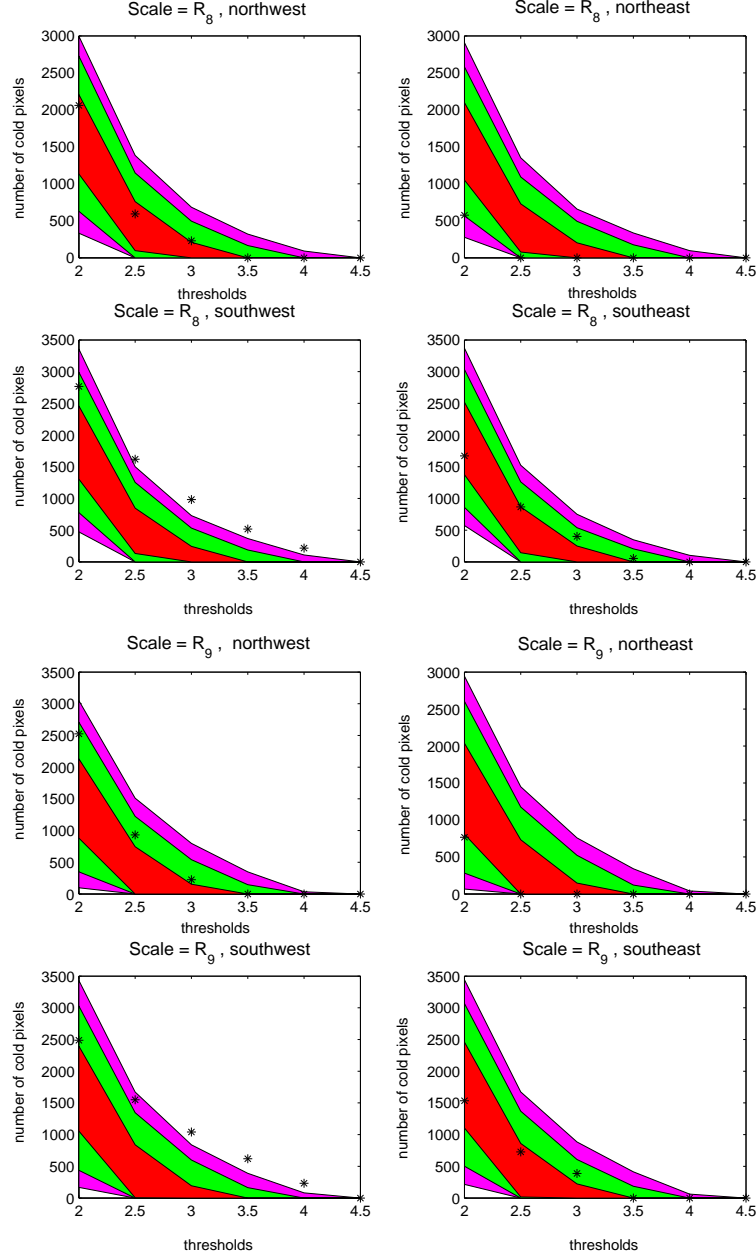


**Figure 6.** Cold area in four regions, scales  $R_8$  and  $R_9$ . The only non-Gaussian region is the southwest. The acceptance intervals are plotted as in Figure 1.

#### 4.4 Skewness and kurtosis

At scales  $R_8$  and  $R_9$ , the kurtosis presented non-Gaussian values in Vielva et al. 2004. We have repeated the analysis of Vielva et al. 2004, masking The Spot in the wavelet coefficient maps, to show to which extent The Spot is responsible for the excess of kurtosis. The masked pixels, were the pixels of The Spot lying above threshold 3.0 at scale  $R_8$ . The results are presented in Figure 9. The stars represent the data and the circles, the data without the Spot. By subtracting The Spot, the decrease of the kurtosis is clearly observed, being now compatible with Gaussianity. The acceptance intervals are the same as in Vielva et al. 2004, and

they were not recalculated masking the pixels of The Spot in the simulations, since the number of masked pixels is negligible with respect to the total number of pixels. However the decrease in the kurtosis is so huge, that a slight modification of the intervals would not affect our conclusions. The skewness is still compatible with Gaussianity. Note that the Spot was masked after convolving with the wavelets. Masking The Spot before convolving, the decrement of the kurtosis is even higher. This results show again the Gaussian behaviour of the data without The Spot. Hence we can conclude that the excess of kurtosis is exclusively due to The Spot.

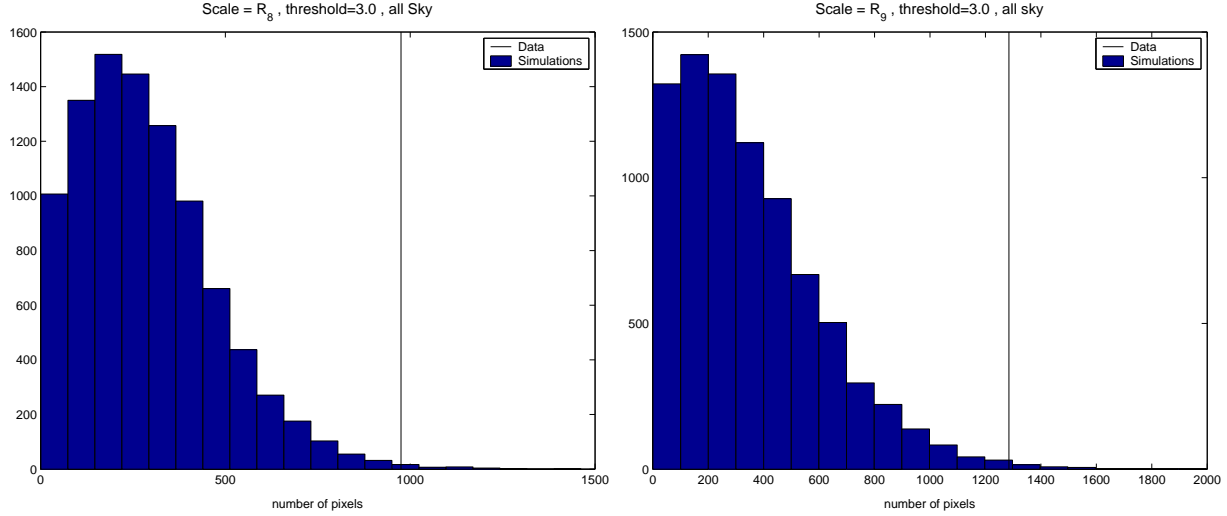


**Figure 7.** Histogram of all biggest cold spots, threshold 3.0, scales  $R_8$  and  $R_9$ . The vertical line represents The Spot.

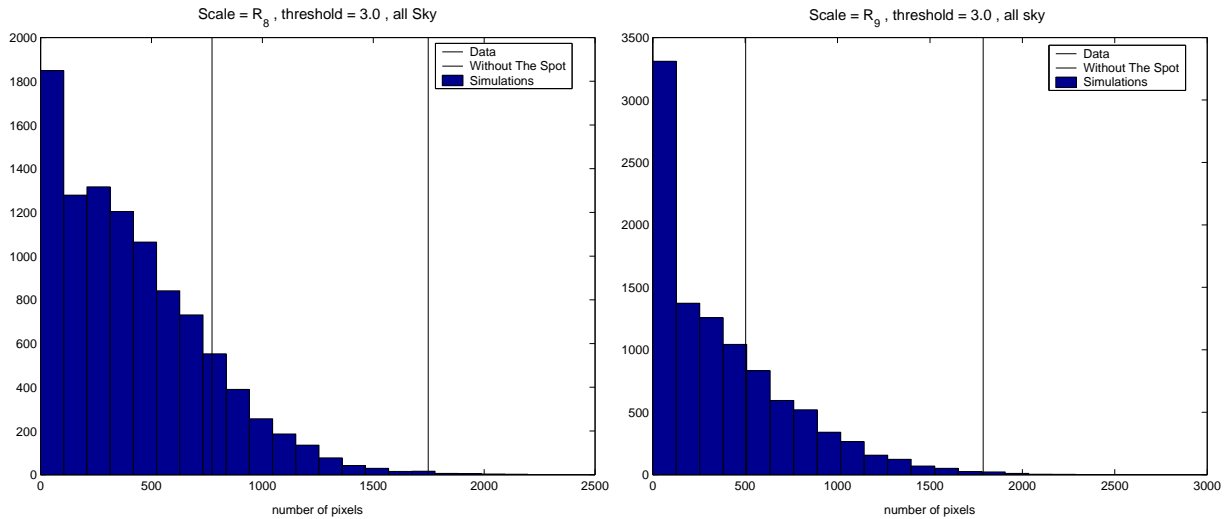


**Figure 8.** Histogram of all cold areas, threshold 3.0, scales  $R_8$  and  $R_9$ . The data without The Spot (line on the left) are compatible with Gaussianity, whereas the data with The Spot (line on the right), are non-Gaussian with probabilities 99.82% and 99.61% at this threshold.

Scale	threshold	probability
$R_8$	3.0	0.34%
	3.5	0.32%
	4.0	0.41%
	4.5	0.65%
$R_9$	3.0	0.38%
	3.5	0.21%
	4.0	0.18%
	4.5	0.22%

**Table 2.** Upper tail probabilities of having The Spot under a Gaussian model, at different scales and thresholds. All probabilities are smaller than 1%.

## 5 SOURCES OF NON-GAUSSIANITY

Although Vielva et al. 2004 showed that systematics, foregrounds and variations of the power spectrum were not responsible for the non-Gaussian effect shown in the kurtosis, we wanted to check again their influence in the non-Gaussian results obtained in the present analysis.

### 5.1 Systematics

First we studied the effects of systematics related to instrumental features (noise and beam), generating four sets of 10 simulations. The first two sets are normal simulations with noise and beams. In the third set we made the same simulations as in the first set but without noise, and in the fourth set we took the simulations of the second but without beam.

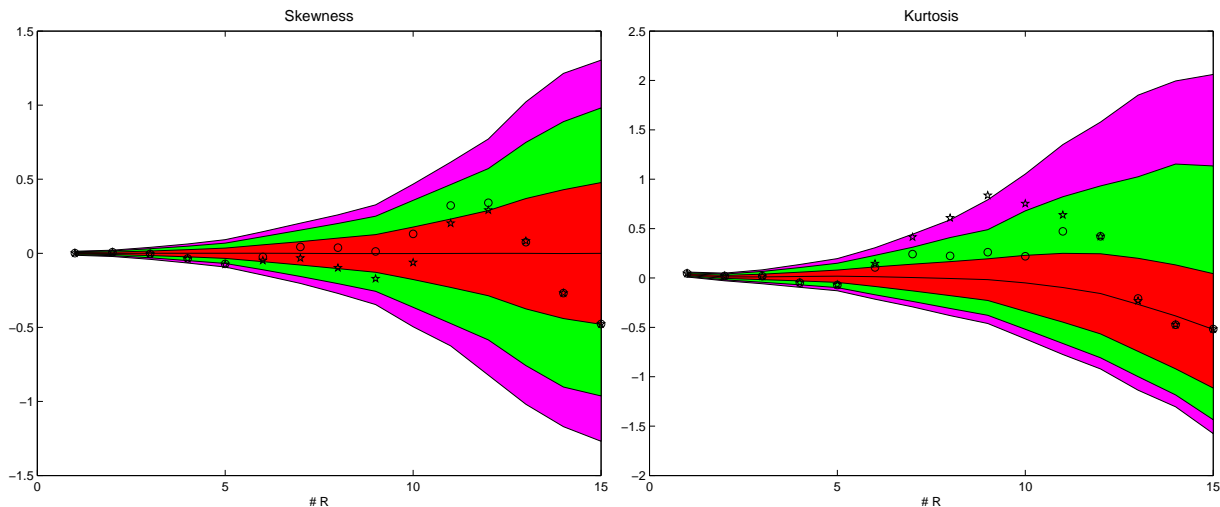


**Figure 9.** This figure shows the values of skewness (left) and kurtosis (right) for all the considered scales. The combined map values are plotted as stars and as written in Vielva et al. 2004, at scales  $R_8$  and  $R_9$  they lie outside the three acceptance intervals, which are represented as in previous figures. Masking those pixels of The Spot which are above threshold 3.0 at scale  $R_8$ , we obtain the results represented by circles. The huge decrement of the kurtosis makes the data compatible with Gaussianity.

Scale	threshold	P with Spot	P without Spot
$R_8$	3.0	0.18%	14.79%
	3.5	0.28%	18.28%
	4.0	0.45%	-
	4.5	0.65%	-
$R_9$	3.0	0.39%	30.53%
	3.5	0.18%	17.68%
	4.0	0.19%	-
	4.5	0.22%	-

**Table 3.** Upper tail probabilities of having the cold area measured in the data, under a Gaussian model. The third column displays the probabilities considering The Spot and the right column shows the probabilities subtracting The Spot from the data. At thresholds 4.0 and 4.5 only The Spot is present, hence it makes no sense considering probabilities without The Spot.

Combined WMAP		
Amplitude ( $\mu K$ )	Position ( $b, l$ )	area ( $\nu = -2$ )
-346	( $-60^\circ, 213^\circ$ )	46
-398	( $-56^\circ, 210^\circ$ )	67
-331	( $-54^\circ, 211^\circ$ )	42
-317	( $-56^\circ, 203^\circ$ )	88
Gaussian ( $4^\circ$ )		
Amplitude ( $\mu K$ )	Position ( $b, l$ )	area ( $\nu = -2$ )
-73	( $-57^\circ, 209^\circ$ )	699

**Table 4.** Before filtering the combined map, The Spot appears resolved in several spots. At the top we show three characteristic values of the most prominent spots, namely the area below threshold -2, amplitude and position of the minimum. Filtering with a Gaussian of  $4^\circ$  all these spots are convolved, becoming one big spot. The characteristics of this spot are shown at the bottom.

Comparing the first and the third set, we can see how the noise affects the number of pixels in a spot or the total cold area, and comparing sets two and four, we check the influence of the beams. We have compared the spots and the total area of these sets at scales  $R_8$  and  $R_9$ , and threshold 3.0. In all cases the mean relative variation of the area of one spot was around 2% and the mean relative variation of the total area in a simulation around 1%. These values are negligible and confirm that noise and beams do not play a significant role in our results, although the number of considered simulations is not very high. The previous results of Vielva et al. 2004 support our conclusions.

Another possible source of non-Gaussianity could be the influence of any rare receiver. We have analyzed the spots detected by the 8 Q-V-W receivers, Q1, Q2, V1, V2, W1, W2, W3 and W4, independently. The results for scales  $R_8$  and  $R_9$  are plotted in Figure 10. Although W2 detects less pixels than the other receivers, all of them detect The Spot, and are close to the line representing the values of the combined map. Hence we verify that our detection is not due to any deficient receiver.

## 5.2 Foregrounds

Non-Gaussianity can be generated by foregrounds due to synchrotron, free-free and thermal dust emissions. All foregrounds show a clear frequency dependence and hence if our Spot is generated by foregrounds its area should also be frequency dependent. Therefore, in Figure 11 we have compared the area of The Spot for each channel, namely K(22.8 GHz), Ka(33.0 GHz), Q(40.7 GHz), V(60.8 GHz) and W(93.5 GHz) at scales  $R_8$  and  $R_9$  and thresholds over 3. The horizontal lines denote the combined map values, whereas the other symbols correspond to the area of The Spot at different thresholds for each channel.

The first two channels are not foreground corrected and so they may not match the results of the other channels

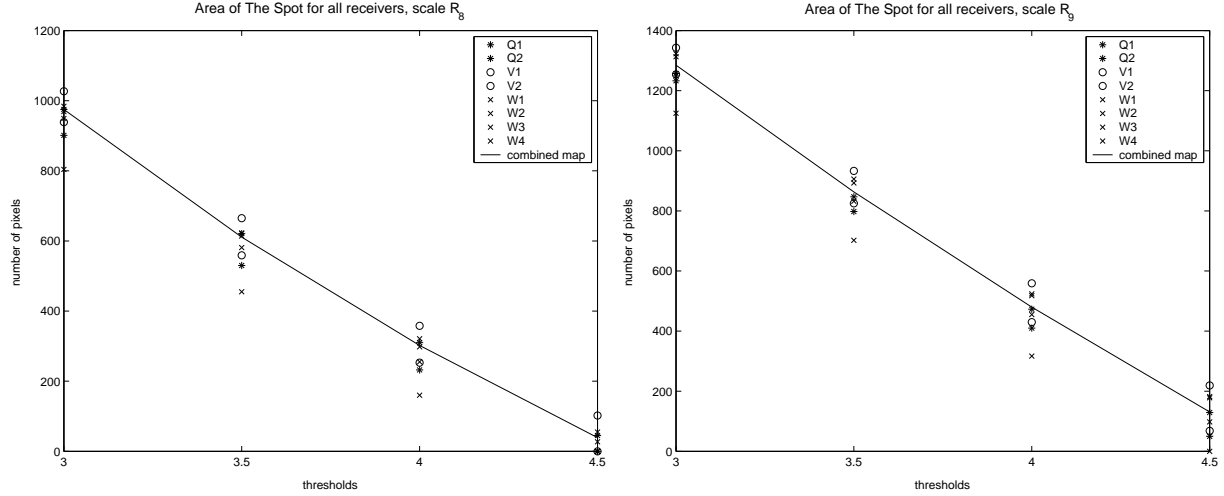


**Figure 10.** Area of The Spot for all receivers, at threshold 3.0 and scales  $R_8$  and  $R_9$ . The line represents the combined map values whereas the other symbols denote the different receivers. The Spot is detected in all receivers, hence no rare receiver is generating the non-Gaussian signal.

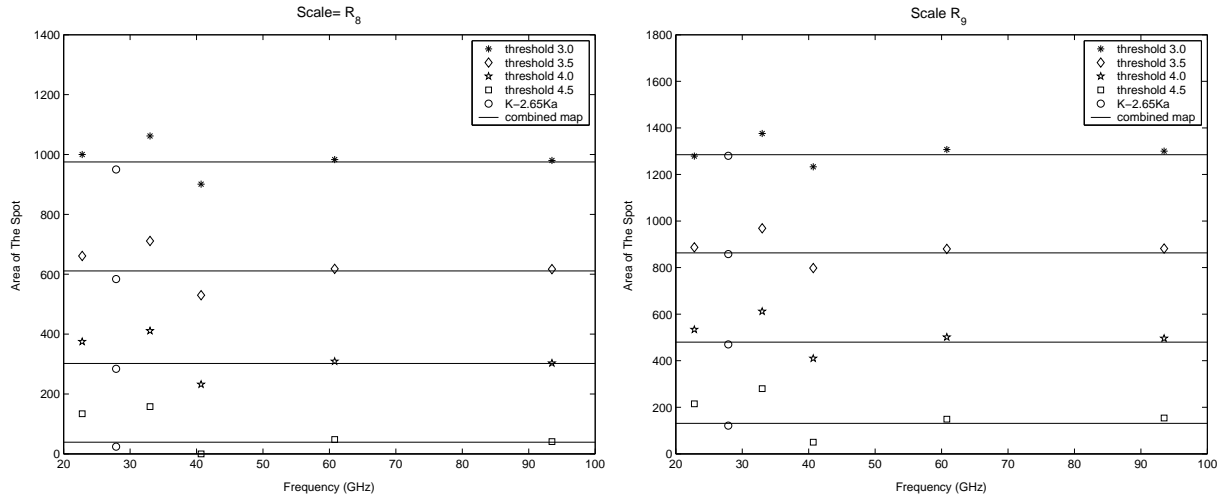


**Figure 11.** Frequency dependence of the area of The Spot, at thresholds over 3.0 and scales  $R_8$  and  $R_9$ . The lines represent the combined map values. From top to bottom thresholds 3.0 (asterisks), 3.5 (diamonds), 4.0 (stars) and 4.5 (squares) are plotted. The circles are the values for the map  $K - 2.65Ka$ , where the synchrotron emission should be canceled. These circles are close to the combined map values, hence synchrotron emission is not the cause of The Spot.

and of the combined map. In fact as can be seen in Figure 11 both channels deviate slightly from the horizontal lines, representing the combined map values. Since these channels are not foreground corrected, we can attribute the deviation to the synchrotron radiation, which dominates at these frequencies. The synchrotron emission is expected to grow a factor 2.65 from 33 GHz to 23 GHz,<sup>‡</sup> hence if we subtract 2.65 times the Ka-map from the K one, we get rid of the

<sup>‡</sup> A power law is assumed for the frequency dependence of the synchrotron emission:  $T_{syn}(\nu) \propto T_{syn}(\nu_0) \left( \nu/\nu_0 \right)^{-2.7}$ , as proposed by Bennett et al. (2003b).

contaminating emission. Considering Figure 11, we confirm that the circles corresponding to  $K - 2.65Ka$  are very close to the combined map values.

These results support the conclusions reached in Vielva et al. 2004 regarding the influence of foregrounds in the non-Gaussian detection. The independence of the amplitude of The Spot with frequency, was already shown in the mentioned paper.

### 5.3 Power spectrum dependence

Since several anomalies and asymmetries have been found in the low multipoles of the power spectrum, we should discuss to which extent the result depends on the power spec-

trum. We have used the best fit WMAP power spectrum to perform the 10000 Gaussian simulations, but the uncertainties in the cosmological parameters and hence in the power spectrum could affect our results. We have performed three sets of 50 simulations. The first set corresponds to the best fit WMAP power spectrum. The other two sets were generated with power spectra differing by  $\pm 1\sigma$  from the best fit WMAP power spectrum. One corresponds to the 'lower limit' power spectrum, obtained subtracting the  $1\sigma$  error estimated by the WMAP team, and the other one to the 'upper limit' power spectrum, adding the mentioned  $1\sigma$  error to the best fit spectrum. Comparing the first set with the two others, we can study how the spots are affected by the choice of different power spectra.

At scales  $R_8$  and  $R_9$ , and threshold 3.0 the mean relative variation of the area of a particular cold spot is much lower than 1%. Therefore, after these negligible variations, the significance of The Spot remains unchanged. Also Vielva et al. 2004 found a negligible power spectrum dependence of the acceptance intervals for the kurtosis. Hence the choice of different power spectra does not affect significantly our results.

#### 5.4 Intrinsic anisotropies

Once we have discarded systematics and foregrounds as the cause of our detection, other sources have to be considered. For instance the Sunyaev-Zeldovich effect could produce a cold spot. This effect occurs in clusters, when high energetic electrons collide with CMB photons originating a decrement of the temperature in our range of frequencies. Here arise two problems, namely the angular scale and the amplitude of The Spot. The non-Gaussianity is found at scales around  $4^\circ$  implying a size of about  $10^\circ$  on the sky. Observing in real space this region, The Spot appears resolved in several smaller very cold spots with a minimum temperature around  $-398\mu K$ . We have looked for any extragalactic object which could cover this angular scale at coordinates near ( $b = -57^\circ, l = 209^\circ$ ). We found a group of galaxies belonging to the local supercluster at a distance of about 20 Mpc subtending a similar angle on the sky. Some of these galaxies match the resolved spots observed in the data. However the mass and temperature of the gas necessary to reach the amplitude of our Spot, are similar to the values found in rich clusters and therefore much higher than the amounts estimated for groups of galaxies (see Taylor et al. 2003). We would need a big cluster, such as the Coma one, to reach such an amplitude and it should be near enough to cover 10 degrees on the sky. In the neighborhood of ( $b = -57^\circ, l = 209^\circ$ ) no such object is found. This is in agreement with the WMAP results on foregrounds (Bennett et al 2003b) where the Sunyaev-Zeldovich effect was found to be negligible except for the most prominent nearby cluster, Coma, observed with a signal to noise ratio of  $\approx 2$ . Even more, we have also considered the ACO catalogue and the All-Sky ROSAT maps (Snowden et al. 1997) at 0.1, 1.2 and 2 keV and neither any ACO cluster nor any special X-ray emission was found at the The Spot position. However, the ROSAT maps present some particular problems: the brightest point sources, as well as a large fraction of clusters, have been removed from it. In addition, some small fractions of

the sky were not observed and, unfortunately, one of them is very close to our object.

Another possible source is the Rees-Sciama effect, (Martínez-González et al. 1990, Martínez-González & Sanz 1990). An extremely massive and distant superstructure would be a clear candidate to cause a cold and big secondary anisotropy. Even topological defects like global monopoles or textures (Turok & Spergel 1990) could have cooled the CMB photons, to produce such spot. Cosmic strings have characteristic scales around arcminutes, hence we do not expect them to be behind this non-Gaussian detection.

## 6 CONCLUSIONS

Motivated by the non-Gaussianity found in the WMAP 1-year data using the SMHW, we have performed an analysis of the spots in the SMHW coefficients map, aimed to locate possible contributors in the sky. An extremely cold and big spot is detected. This spot (*The Spot*) is seen in the SMHW coefficients at scales around  $4^\circ$  (implying a size of around  $10^\circ$  on the sky) and at Galactic coordinates  $b = -57^\circ, l = 209^\circ$ . The probability of having such spot for a Gaussian model is of only  $\approx 0.2\%$ , which implies that, if intrinsic, The Spot has not been originated by primary anisotropies in the standard scenario of structure formation since standard inflation predicts Gaussian fluctuations in the matter energy density and therefore in the CMB temperature fluctuations. When this spot is not considered in the analysis the rest of the data seem to be consistent with Gaussianity.

In order to identify the source of The Spot we have performed several tests related to systematic effects and foregrounds. We have checked that uncertainties in the noise or in the beam response have a negligible effect in our results at the relevant wavelet scales. Looking at the maps corresponding to the different receivers, we see a clear consistency in the area, amplitude and position of The Spot. Hence our detection is not due to any deficient receiver. In relation to the possible foregrounds contribution, we have looked for possible frequency dependences in the amplitude and area of The Spot. Again both quantities show a nice consistency with a constant line in the range from 23 to 94 GHz. Whereas the Galactic foregrounds show a very different frequency dependence with respect to the constant behaviour, the SZ effect does not separate much from it in that frequency range. A comparable spot could be produced either by the Coma cluster at a much closer distance, or by several rich clusters at the actual distance of Coma. We have checked that no nearby rich cluster of galaxies is located in the position of The Spot.

Finally, intrinsic fluctuations cannot be rejected as the source of The Spot. In particular, a massive and distant super-structure could in principle produce a decrement as the one observed through the Rees-Sciama effect (Martínez-González and Sanz 1990). This massive structure (of order of at least  $10^{16}M_\odot$ ) should be placed far enough because otherwise it would have been detected previously. Alternatively, more speculative possibilities are topological defects (monopoles or textures) or non-standard inflationary scenarios. Even more, a combination of secondary anisotropies with primary ones, cannot be rejected as the source of our non-Gaussian spot. For instance a possibility could be a

combination of the Sunyaev-Zeldovich effect with a Sachs-Wolfe plateau.

## ACKNOWLEDGMENTS

Authors kindly thank J. M. Diego for very useful discussions about the Sunyaev-Zeldovich effect in the local galaxy distribution, C. Hernández-Monteaudo for helpful comments about the ACO catalog and R. Durrer for comments on topological defects. MC thanks Spanish Ministerio de Educacion Cultura y Deporte (MECD) for a predoctoral FPU fellowship. PV acknowledges support from IN2P3 (CNRS) for a post-doc fellowship. We acknowledge partial financial support from the Spanish MCYT project ESP2002-04141-C03-01. We kindly thank IFCA for providing us with its Grid Wall cluster to generate and analyze the WMAP simulations. We thank the RTN of the EU project HPRN-CT-2000-00124 for partial financial support. We acknowledge the use of the Legacy Archive for Microwave Background Data Analysis (LAMBDA). Support for LAMBDA is provided by the NASA Office of Space Science. This work has used the software package HEALPix (Hierarchical, Equal Area and iso-latitude pixelization of the sphere, <http://www.eso.org/science/healpix>), developed by K.M. Górski, E. F. Hivon, B. D. Wandelt, J. Banday, F. K. Hansen and M. Barthelmann. We acknowledge the use of the software package CMBFAST (<http://www.cmbfast.org>) developed by U. Seljak and M. Zaldarriaga.

## REFERENCES

- Acquaviva V., Bartolo N., Matarrese S. & Riotto A., 2003, *Nucl.Phys.* B667 119-148
- Aghanim N., Desert F. X., Puget J. L. & Gispert R., 1996, *A&A*, 311, 1
- Aghanim N., Kunz M., Castro P. G. & Forni O., 2003, *A&A*, 406, 797
- Antoine J. P. & Vanderheynt P., 1998, *J. Math Phys.*, 39, 3987
- Barreiro R. B., Hobson M. P., Lasenby A. N., Banday A. J., Górski K. M. & Hinshaw G., 2000, *MNRAS*, 318, 475
- Barreiro R. B. & Hobson M. P., 2001, *MNRAS*, 327, 813
- Bennett C. L. et al., 2003a, *ApJS*, 148, 1
- Bennett C. L. et al., 2003b, *ApJS*, 148, 97
- Bernardeau F., Uzan J.-P., 2002, *Phys. Rev. D*, 66, 103506
- Cayón L., Sanz J. L., Barreiro R. B., Martínez-González E., Vielva P., Toffolatti L., Silk J., Diego J. M. & Argüeso F., 2000, *MNRAS*, 315, 757
- Cayón L., Sanz J. L., Martínez-González E., Banday A. J., Argüeso F., Gallegos J. E., Górski K. M. & Hinshaw G., 2001, *MNRAS*, 326, 1243
- Cayón L., Martínez-González E., Argüeso F., Banday A. J. & Górski K. M., 2003, *MNRAS*, 339, 1189
- Chiang L. -Y., Naselsky P. D., Verkhodanov O. V. & Way M. J., 2003, *ApJ*, 590, L65
- Copí C.J., Huterer D., Starkman G.D., 2003, preprint (astro-ph/0310511)
- Durrer R., 1999, *New Astron. Rev.*, 43, 111
- Eriksen H. K., Hansen F. K., Banday A. J., Górski K. M. & Lilje P. B., 2004, *ApJ*, 605, 14
- Eriksen H. K., Banday A.J., Górski K.M., Lilje P.B, 2004, preprint (astro-ph/0403098)
- Eriksen H. K., Novikov D. I., Lilje P. B., Banday A. J. & Górski K. M., 2004, *ApJ*, submitted (astro-ph/0401276)
- Goldberg D. M. & Spergel D. N., 1999, *Phys. Rev.*, D59, 103002
- Górski K. M., Wandelt B. D., Hansen F. K., Hivon E. & Banday A. J., 1999, (astro-ph/9905275)
- Hansen F.K., Cabella P., Marinucci D., Vittorio N., 2004, preprint (astro-ph/0402396)
- Hansen F.K., Banday A.J. , Górski K.M., 2004, preprint (astro-ph/0404206)
- Hobson M. P., Jones A. W. & Lasenby A. N. 1999, *MNRAS*, 309, 125
- Hu W., 2000, *Phys. Rev.*, D62, 043007
- Komatsu E. et al., 2003, *ApJS*, 148, 119
- Larson D.L., Wandelt B.D., 2004, preprint (astro-ph/0401623)
- Linde A. & Mukhanov V., 1997, *Phys. Rev.*, D56, 535
- Martínez-González E. & Sanz J. L., 1990, *MNRAS*, 247, 473
- Martínez-González E., Sanz J. L. & Silk J., 1990, *MNRAS*, 247, 473
- Martínez-González E., Sanz J. L. & Cayón L., 1997, *ApJ*, 484, 1
- Martínez-González E., Gallegos J. E., Argüeso F., Cayón L. & Sanz J. L., 2002, *MNRAS*, 336, 22
- Mukherjee P. & Wang Y., 2004, *ApJ* accepted, (astro-ph/0402602)
- Ostriker J. P. & Vishniac E. T., 1986, *ApJ*, 306, L51
- Pando J., Valls-Gabaud D. & Fang L. -Z., 1998, *Phys. Rev. Lett.*, 81, 4568
- Park C. G. 2004, *MNRAS* 349, 313-320
- Peebles P. J. E., 1997, *ApJ*, 483, 1
- Rees M. J. & Sciama D. W., 1968, *Nature*, 517, 611
- Sanz J. L., Argüeso F., Cayón L., Martínez-González E., Barreiro R. B. & Toffolatti L., 1999a, *MNRAS*, 309, 672
- Sanz J. L., Barreiro R. B., Cayón L., Martínez-González E., Ruiz G. A., Díaz F. J., Argüeso F., Silk J. & Toffolatti L., 1999b, *A&AS*, 140, 99
- Seljak U. & Zaldarriaga M., 1996, *ApJ*, 469, 437.
- Snowden S. L., Egger R., Freyberg M. J., McCammon D., Plucinsky P. , Sanders W. T., Schmitt J. H. M. M., Truemper J., Voges W., 1997, *ApJ*, 485, 125
- Spergel D. N. et al., 2003, *ApJS*, 148, 175
- Taylor, J.E., Moodley, K, Diego, J.M., 2003, *MNRAS*, 345, 1127
- Turok N. & Spergel D. N., 1990, *Phys. Rev. Letters*, 64, 2736
- Tenorio L., Jaffe A. H., Hanany S. & Lineweaver C. H., 1999, *MNRAS*, 310, 823
- Vielva P., Martínez-González E., Cayón L., Diego J. M., Sanz J. L. & Toffolatti L., 2001a, *MNRAS*, 326, 181
- Vielva P., Barreiro R. B., Hobson M. P., Martínez-González E., Lasenby A. N., Sanz J. L. & Toffolatti L., 2001b, *MNRAS*, 328, 1
- Vielva P., Martínez-González E., Gallegos J. E., Toffolatti L. & Sanz J. L., 2003, *MNRAS*, 344, 89
- Vielva P., Martínez-González E., Barreiro R.B., Sanz J.L., Cayón L., 2003, *ApJ*, 609, 22